Chapter 7

APPLICATION: FLOW ON THE SURFACE OF A SPHERE

In this chapter we apply the previously developed wave propagation method with constrained transport to the problem of flow on the surface of a sphere. The strategy is to divide the sphere into several curved manifolds which communicate by means of appropriate boundary conditions. On each manifold we apply the generalized coordinate extension of the wave propagation method. In particular, we present numerical solutions to the advection equation in an incompressible velocity field, the classical shallow water equations, and the shallow water magnetohydrodynamic equations.

7.1 Motivation

The aim of large-scale geophysical fluid dynamics is to be able to solve and understand equations related to fluid dynamics on the surface of a rotating planet. The spherical geometry introduced in this framework presents a difficulty that has been considered using several different numerical approaches on several different types of numerical grids. In particular, methods that are based on logically Cartesian grids are faced with the inevitable "pole problem" which results from the introduction of grid singularities that do not correspond to physical singularities. For example, if a regular longitude-latitude grid is chosen, then singularities are introduced at the North and South Poles.

The types of numerical methods that have been used include spectral methods [11, 80, 81, 86, 87, 88], finite-element methods [18], Lagrange-Galerkin methods [31], discontinuous Galerkin methods [33], spectral element methods [32], semi-Lagrangian methods [17, 64], finite difference methods [75, 79], finite difference composite methods [62], finite volume methods on icosahedral grids [36, 37, 92], high-resolution finite volume methods [47, 59], and many more. Each of these methods has certain advantages and disadvantages depending the applications of interest.

In this work, we are particularly interested in magnetohydrodynamics and in accurately capturing shocks and other discontinuities that may form. Because of this we will make use of the high-resolution finite volume framework. Furthermore, we will restrict ourselves to a series of logically Cartesian grids or *patches* that will be used to cover the entire sphere. To overcome the possibly severe singularities that this may introduce, one must carefully choose an appropriate numerical grid. In an early paper on large-scale weather prediction, Phillips [69] outlined the following criteria for developing a useful grid mapping to spherical geometry (as quoted in [75]):

1. The mapping should be free of any singularities.
2. The mapping should preserve the general form of the hydrodynamic equations.
3. The physical grid defined on the spherical surface should be as close as possible to a regular equidistant grid.

4. The equator should be a coordinate line of the grid network.

The algorithm we propose should also have the following three qualities which are the standard benefits that current high-resolution schemes provide:

5. The numerical scheme should be conservative.
6. The numerical scheme should be non-oscillatory in regions of large gradients and near shock waves and other discontinuities.
7. The numerical scheme should be at least $O(\Delta x^2, \Delta t^2)$ in regions where the solution is smoothly varying.

The method of choice for dealing with the above restrictions is the wave propagation method on curved manifolds (see Chapter 6) and is similar to the method presented in [59].

We will in this chapter solve three different hyperbolic equations on the surface of a sphere. These equations and the physical applications they model are as follows:

1. **The advection equation in an incompressible velocity field:** a model for tracer transport such as various kinds of pollutants in the atmosphere.

2. **The classical shallow water equations:** a hydrostatic, single-layer model of the atmosphere.

3. **The magnetohydrodynamic shallow water equations:** a hydrostatic, single-layer model of the solar tachocline.

The advection equation and the classical shallow water equations have been used as tests for numerical methods that are designed for solving the more complicated equations found in global circulation models (GCMs) of the atmosphere. In this chapter we will apply the wave propagation method to a few of the standard test cases that can be found in the atmospheric sciences literature [93] as well as to the more complicated SMHD equations.

7.2 The cubed sphere grid

The numerical grid which we consider is based on a grid mapping which maps the surface of a sphere to the six faces of a cube. In the literature this approach has been referred to as the "cubed sphere" approach [75]. This idea was first introduced in a 1972 paper by Sadourny [79]. Sadourny [79] applies a standard finite difference method to solve the shallow water equations, but concludes that further work must be done to reduce inaccuracies near the "edges" and "corners" the cube. As a result of this conclusion and because during this time spectral methods were shown to produce accurate results with good efficiency [11], very little attention was given to the cubed sphere approach for more than two decades.

It was not until the 1990's that the global dynamics community found renewed interest in finite difference methods. This renewed interest has led to a re-evaluation of the cubed sphere grids first presented by Sadourny [79]. As it currently stands, there are two types of

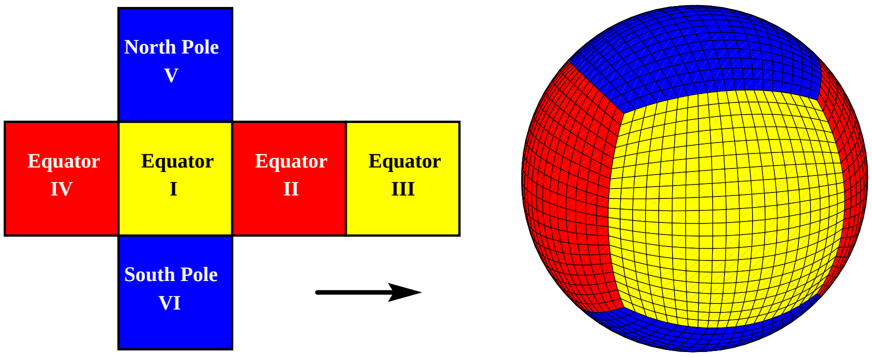

Figure 7.1: The gnomonic grid mapping maps the six faces of a cube to the surface of a sphere. This mapping is nonorthogonal and generates a grid that varies less than 30% in grid cell area.

cubed sphere grids: the conformal cubed sphere [64, 72, 73] and the gnomonic cubed sphere [73, 75].

Spherical coordinates describe an orthogonal coordinate system with a metric tensor given by

$$\boldsymbol{h} = \begin{bmatrix} r^2\cos^2(\lambda) & 0 & 0 \\ 0 & r^2 & 0 \\ 0 & 0 & 1 \end{bmatrix}. \tag{7.1}$$

The advantage of the conformal cubed sphere mapping is that it preserves the orthogonality of the coordinate system. This minimizes the additional geometric terms that appear in the partial differential equations which are being solved. The disadvantage with this approach is that the grid cell area is far from uniform. In fact, as the grid resolution increases, the area ratio of the smallest cell to the largest cell approaches zero. Because of the non-uniformity of the numerical grid, the smallest grid cells will dictate the time step for an explicit scheme; and therefore, the overall accuracy of the method will be significantly reduced. The conformal cubed sphere is therefore not a viable option for explicit time stepping methods [64].

The gnomonic grid mapping divides the sphere into six regions, each generated by taking grid points to be the intersection of great circles passing through the "north" and "south" poles with great circles passing through the "east" and "west" poles relative to that region (see Figure 7.2(a)). Doing this for each region generates six equal grids which cover the entire sphere without overlap. This mapping is illustrated in Figure 7.1. An advantage of this grid mapping is that the variation in grid cell area is fairly small. The area ratio of the smallest to the largest grid cell converges to $\sqrt{2}/2 \approx 0.7071$ as the grid resolution goes to infinity; and furthermore, for a finite grid resolution this ratio is always larger than $\sqrt{2}/2$. We illustrate this point in Figure 7.2(b). Note that the smallest grid cells occur at the

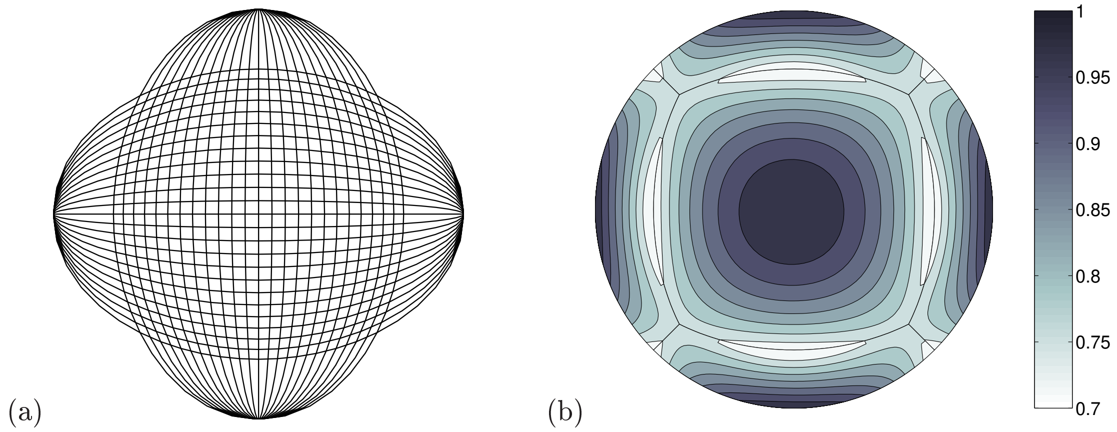

Figure 7.2: (a) A single grid patch is constructed by taking the intersection of a set of angularly equidistant great circles clamped down at the "north" and "south" poles relative to that patch with a set of angularly equidistant great circles clamped down at the the "east" and "west" poles relative to that patch. (b) A plot of the cell area normalized by the largest grid cell.

interface between two grid patches. The disadvantage with the gnomonic grid mapping is that it is a non-conformal mapping and the resulting coordinate system is non-orthogonal.

7.2.1 Grid transformations

The spherical coordinates are denoted by (ϕ, λ, r), where $\phi \in [-\pi, \pi]$ is the longitude, $\lambda \in [-\pi/2, \pi/2]$ is the latitude, and $r =$ constant is the radius of the sphere. On each grid patch the computational domain is given by

$$(\xi, \eta) \in \left[-\frac{\pi}{4}, \frac{\pi}{4}\right] \times \left[-\frac{\pi}{4}, \frac{\pi}{4}\right] . \tag{7.2}$$

Furthermore, we define the following quantities:

$$\alpha_1 \equiv \tan(\xi) \tag{7.3}$$
$$\alpha_2 \equiv \tan(\eta) \tag{7.4}$$
$$\delta \equiv 1 + \alpha_1^2 + \alpha_2^2 \tag{7.5}$$
$$\beta_1 \equiv \sqrt{1 + \alpha_1^2} \tag{7.6}$$
$$\beta_2 \equiv \sqrt{1 + \alpha_2^2} \, . \tag{7.7}$$

Using these definitions, the coordinate transformations (as taken from [75]), the Jacobian matrices, and the metric tensors for each grid patch are given by the following:

<u>Patch 1 (Equator),</u>

$$\alpha_1 = \tan(\phi) \tag{7.8}$$

$$\alpha_2 = \frac{\tan(\lambda)}{\cos(\phi)} \tag{7.9}$$

$$\begin{bmatrix} V_\phi \\ V_\lambda \end{bmatrix} = J_1 \begin{bmatrix} V_\xi \\ V_\eta \end{bmatrix} = \frac{1}{\delta} \begin{bmatrix} \delta & 0 \\ -\alpha_1\alpha_2\beta_1 & \beta_1\beta_2^2 \end{bmatrix} \begin{bmatrix} V_\xi \\ V_\eta \end{bmatrix} \tag{7.10}$$

$$\boldsymbol{h}_1 = J_1^t \begin{bmatrix} r^2\cos^2(\lambda) & 0 \\ 0 & r^2 \end{bmatrix} J_1\,, \tag{7.11}$$

<u>Patch 2 (Equator),</u>

$$\alpha_1 = -\frac{1}{\tan(\phi)} \tag{7.12}$$

$$\alpha_2 = \frac{\tan(\lambda)}{\sin(\phi)} \tag{7.13}$$

$$\begin{bmatrix} V_\phi \\ V_\lambda \end{bmatrix} = J_2 \begin{bmatrix} V_\xi \\ V_\eta \end{bmatrix} = \frac{1}{\delta} \begin{bmatrix} \delta & 0 \\ -\alpha_1\alpha_2\beta_1 & \beta_1\beta_2^2 \end{bmatrix} \begin{bmatrix} V_\xi \\ V_\eta \end{bmatrix} \tag{7.14}$$

$$\boldsymbol{h}_2 = J_2^t \begin{bmatrix} r^2\cos^2(\lambda) & 0 \\ 0 & r^2 \end{bmatrix} J_2\,, \tag{7.15}$$

<u>Patch 3 (Equator),</u>

$$\alpha_1 = \tan(\phi) \tag{7.16}$$

$$\alpha_2 = -\frac{\tan(\lambda)}{\cos(\phi)} \tag{7.17}$$

$$\begin{bmatrix} V_\phi \\ V_\lambda \end{bmatrix} = J_3 \begin{bmatrix} V_\xi \\ V_\eta \end{bmatrix} = \frac{1}{\delta} \begin{bmatrix} \delta & 0 \\ -\alpha_1\alpha_2\beta_1 & \beta_1\beta_2^2 \end{bmatrix} \begin{bmatrix} V_\xi \\ V_\eta \end{bmatrix} \tag{7.18}$$

$$\boldsymbol{h}_3 = J_3^t \begin{bmatrix} r^2\cos^2(\lambda) & 0 \\ 0 & r^2 \end{bmatrix} J_3\,, \tag{7.19}$$

<u>Patch 4 (Equator),</u>

$$\alpha_1 = -\frac{1}{\tan(\phi)} \tag{7.20}$$

$$\alpha_2 = -\frac{\tan(\lambda)}{\sin(\phi)} \tag{7.21}$$

$$\begin{bmatrix} V_\phi \\ V_\lambda \end{bmatrix} = J_4 \begin{bmatrix} V_\xi \\ V_\eta \end{bmatrix} = \frac{1}{\delta} \begin{bmatrix} \delta & 0 \\ -\alpha_1\alpha_2\beta_1 & \beta_1\beta_2^2 \end{bmatrix} \begin{bmatrix} V_\xi \\ V_\eta \end{bmatrix} \tag{7.22}$$

$$\boldsymbol{h}_4 = J_4^t \begin{bmatrix} r^2\cos^2(\lambda) & 0 \\ 0 & r^2 \end{bmatrix} J_4\,, \tag{7.23}$$

<u>Patch 5 (North Pole),</u>

$$\alpha_1 = \frac{\sin(\phi)}{\tan(\lambda)} \tag{7.24}$$

$$\alpha_2 = -\frac{\cos(\phi)}{\tan(\lambda)} \tag{7.25}$$

$$\begin{bmatrix} V_\phi \\ V_\lambda \end{bmatrix} = J_5 \begin{bmatrix} V_\xi \\ V_\eta \end{bmatrix} = \frac{-1}{\delta(\delta-1)} \begin{bmatrix} \delta\alpha_2\beta_1^2 & -\delta\alpha_1\beta_2^2 \\ \alpha_1\beta_1^2\sqrt{\delta-1} & \alpha_2\beta_2^2\sqrt{\delta-1} \end{bmatrix} \begin{bmatrix} V_\xi \\ V_\eta \end{bmatrix} \tag{7.26}$$

$$\boldsymbol{h}_5 = J_5^t \begin{bmatrix} r^2\cos^2(\lambda) & 0 \\ 0 & r^2 \end{bmatrix} J_5\,, \tag{7.27}$$

<u>Patch 6 (South Pole),</u>

$$\alpha_1 = -\frac{\sin(\phi)}{\tan(\lambda)} \tag{7.28}$$

$$\alpha_2 = -\frac{\cos(\phi)}{\tan(\lambda)} \tag{7.29}$$

$$\begin{bmatrix} V_\phi \\ V_\lambda \end{bmatrix} = J_6 \begin{bmatrix} V_\xi \\ V_\eta \end{bmatrix} = \frac{1}{\delta(\delta-1)} \begin{bmatrix} \delta\alpha_2\beta_1^2 & -\delta\alpha_1\beta_2^2 \\ \alpha_1\beta_1^2\sqrt{\delta-1} & \alpha_2\beta_2^2\sqrt{\delta-1} \end{bmatrix} \begin{bmatrix} V_\xi \\ V_\eta \end{bmatrix} \tag{7.30}$$

$$\boldsymbol{h}_6 = J_6^t \begin{bmatrix} r^2\cos^2(\lambda) & 0 \\ 0 & r^2 \end{bmatrix} J_6\,. \tag{7.31}$$

In addition to the above grid transformations, it will often be necessary to compute the distance between two points on the surface of a sphere of radius r. The shortest distance between two points (ϕ, λ) and (ϕ_0, λ_0) is obtained by taking the great circle that passes through both points and then computing the shorter arc length between the two points on the great circle:

$$\mathbf{dist}\big[\,(\phi,\lambda) \leftrightarrow (\phi_0,\lambda_0)\,\big] \equiv r\cos^{-1}\Big\{\cos(\lambda)\cos(\lambda_0)\cos(\phi-\phi_0) + \sin(\lambda)\sin(\lambda_0)\Big\}\,. \tag{7.32}$$

7.2.2 Boundary conditions

The gnomonic grid mapping provides us with a nearly uniform grid on the surface of a sphere and eliminates the grid singularities introduced by the latitude-longitude grid. In turn we are faced with two new difficulties:

1. The underlying metric is non-orthogonal.

2. Artificial boundaries between the six grid patches have been created.

Although the equations are somewhat more complicated in a non-orthogonal coordinate system, the numerical method introduced in Chapter 6 of this work was developed to handle

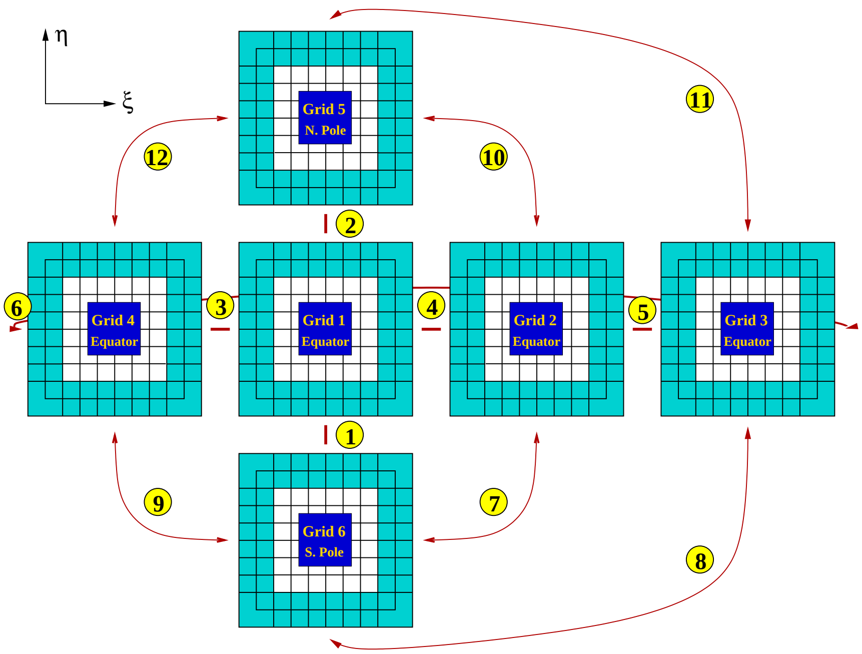

Figure 7.3: Appropriate boundary conditions must be applied to all 12 interfaces of the cubed sphere grid. Note that across interfaces 7 through 12 the grid patch orientation changes.

general metric tensors. This leaves us only with the second challenge of dealing with the artificial boundaries between grid patches.

Philosophically, we can think of solving the governing partial differential equation on each of the six grid patches as separate problems. Each grid patch has its own interior grid cells, its own (ξ, η) coordinate system, and two layers of *ghost cells* as required by the wave propagation method [53]. Information is passed between grid patches by placing the appropriate boundary conditions into the ghost cells. Note that the indexing may change from one grid patch to the next. This scenario is depicted in Figure 7.3.

A grid cell on a general curved manifold is defined by an index (ij), a grid center (ξ_i, η_j), and a solution value (Q_{ij}). Before we can place solution value information into the ghost cells, we must first decide how to define the geometry of the ghost cells. The two obvious choices for the ghost cell geometry are as follows:

Option 1: Let the ghost cells have the same shape as the grid cells from the neighboring grid patch and directly copy solution values into these cells.

Option 2: Extend the coordinate lines of the current grid patch and apply interpolation techniques to approximate the solution values in these cells.

These two options are illustrated in Figure 7.4.

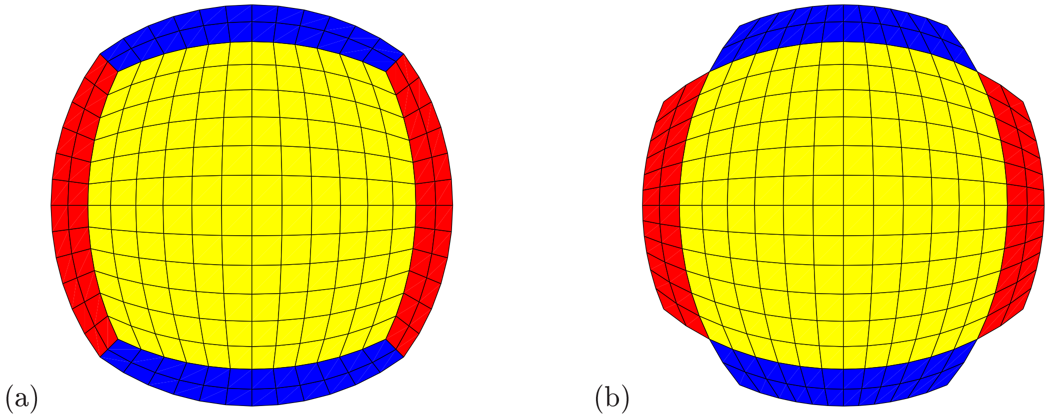

Figure 7.4: Two types of boundary conditions for the six sphere patches: (a) Ghost cells are one and the same as grid cells on neighboring patches. No interpolation is required to obtain the solution values (Q_{ij}) in these ghost cells. (b) Ghost cells are obtained by extending the current grid onto the neighboring patch. Solution values (Q_{ij}) are placed into these ghost cells by one-dimensional interpolation.

The first option is attractive because the ghost cells and the neighboring grid patch identically match, meaning that no interpolation is required to place solution values (Q_{ij}) into the ghost cells. The disadvantage with this approach is that ghost cell information and interior grid information will be in different coordinate systems. For vector conservation laws this turns out to be very restrictive.

On the other hand, the second option allows to keep the ghost cells and interior cells in the same coordinate system. The price we pay is that there is now non-trivial overlap between ghost cells and the neighboring grid patch, forcing us to use interpolation techniques to obtain solution values for the ghost cells. It turns out, however, that the overlap is such that only one-dimensional interpolation is required (see [75]). It is this second option that is favored in the literature (see for example [62, 75]).

In this work we will make use of both of the above options depending on the equations that are being solved:

1. The advection equation: Option 1

2. The shallow water equations: Option 2

3. The SMHD equations: Option 2.

The advection equation can be described entirely by two scalars: the concentration ($q(\xi, \eta\, t)$) and the streamfunction ($\Psi(\xi, \eta, t)$). Because scalars are coordinate independent we favor

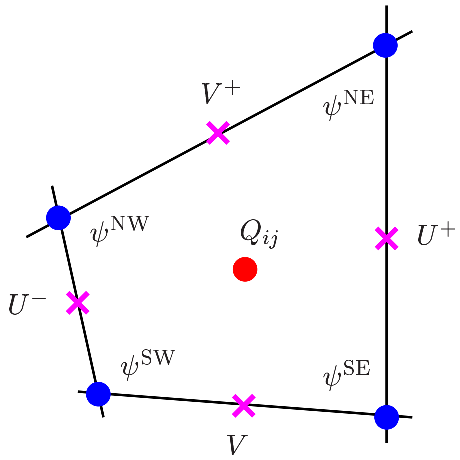

Figure 7.5: Staggered grid for the advection equation in generalized coordinates.

the first option. Furthermore, the use of Option 1 will guarantee the numerical conservation of $q(\xi, \eta, t)$ across grid patches. In solving the shallow water and SMHD equations we will make use of Option 2. In order to guarantee the conservation of mass accross grid patches, we must make sure that the numerical mass flux on either side of the grid interface are equal. This accomplished by simple averaging:

$$F_{\mathrm{left}} \longrightarrow \frac{1}{2}\left(F_{\mathrm{left}} + F_{\mathrm{right}}\right) \tag{7.33}$$

$$F_{\mathrm{right}} \longrightarrow \frac{1}{2}\left(F_{\mathrm{left}} + F_{\mathrm{right}}\right) . \tag{7.34}$$

Since the momentum is not conserved due to the geometric source term, we do not impose this condition on the momentum flux.

7.3 Advection on the sphere

The two-dimensional incompressible advection equation in the generalized coordinates (ξ, η) is given by

$$\partial_t \left(\kappa q\right) + \kappa u_1 \partial_\xi q + \kappa u_2 \partial_\eta q = 0 \tag{7.35}$$

$$\partial_\xi \left(\kappa u_1\right) + \partial_\eta \left(\kappa u_2\right) = 0 \, . \tag{7.36}$$

Because the velocity field is incompressible we can define a streamfunction $\Psi(\xi, \eta)$ as follows:

$$\partial_\eta \Psi = \kappa u_1 \tag{7.37}$$

$$\partial_\xi \Psi = -\kappa u_2 \, . \tag{7.38}$$

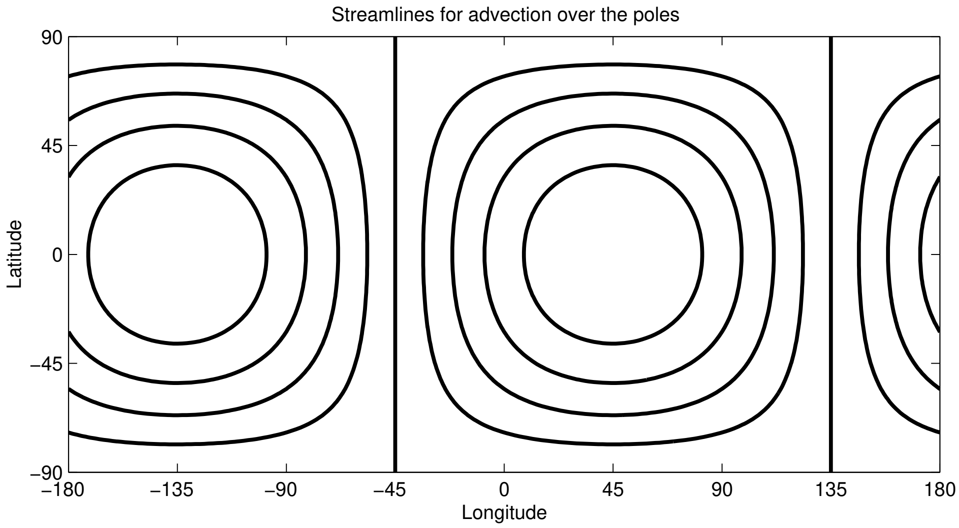

Figure 7.6: The stream function for advection over the poles along the great circle which is aligned with the $\phi = -45°$ and $\phi = 135°$ coordinate lines.

As in Section 2.5, we define a grid staggering such that the streamfunction is evaluated at cell corners and the concentration at cell centers. The velocities are defined at cell edges and are computed by applying the second order centered finite differences to the streamfunction:

$$[\kappa u_1]_{i-1/2,j} = \frac{\Psi_{i-1/2,j+1/2} - \Psi_{i-1/2,j-1/2}}{\Delta\eta} \tag{7.39}$$

$$[\kappa u_2]_{i,j-1/2} = \frac{\Psi_{i-1/2,j-1/2} - \Psi_{i+1/2,j-1/2}}{\Delta\xi}\,. \tag{7.40}$$

We illustrate the above grid staggering on a logically rectangular grid in Figure 7.5. This grid staggering coupled with the streamfunction differencing in (7.39) and (7.40) guarantees that the following discrete approximation to $\nabla \cdot \mathbf{u}$ is identically zero:

$$[\nabla \cdot \mathbf{u}]_{ij} \approx \frac{[\kappa u_1]_{i+1/2,j} - [\kappa u_1]_{i-1/2,j}}{\Delta\xi} + \frac{[\kappa u_2]_{i,j+1/2} - [\kappa u_2]_{i,j-1/2}}{\Delta\eta} = 0\,. \tag{7.41}$$

This condition also guarantees that $q(\xi, \eta, t)$ is numerically conserved. Below we apply this method on the cubed sphere geometry discussed at the beginning of this chapter.

7.3.1 Example: advection of a cosine bell over the poles

We begin by considering problem #1 of the Williamson et al. [93] test suite on a sphere of radius $r = 1$. The initial concentration in spherical coordinates is given by

$$q(\phi, \lambda, 0) = \begin{cases} 0.5\big(1 + \cos(3\pi s)\big) & \text{if } s < 1/3 \\ 0 & \text{otherwise}\,, \end{cases} \tag{7.42}$$

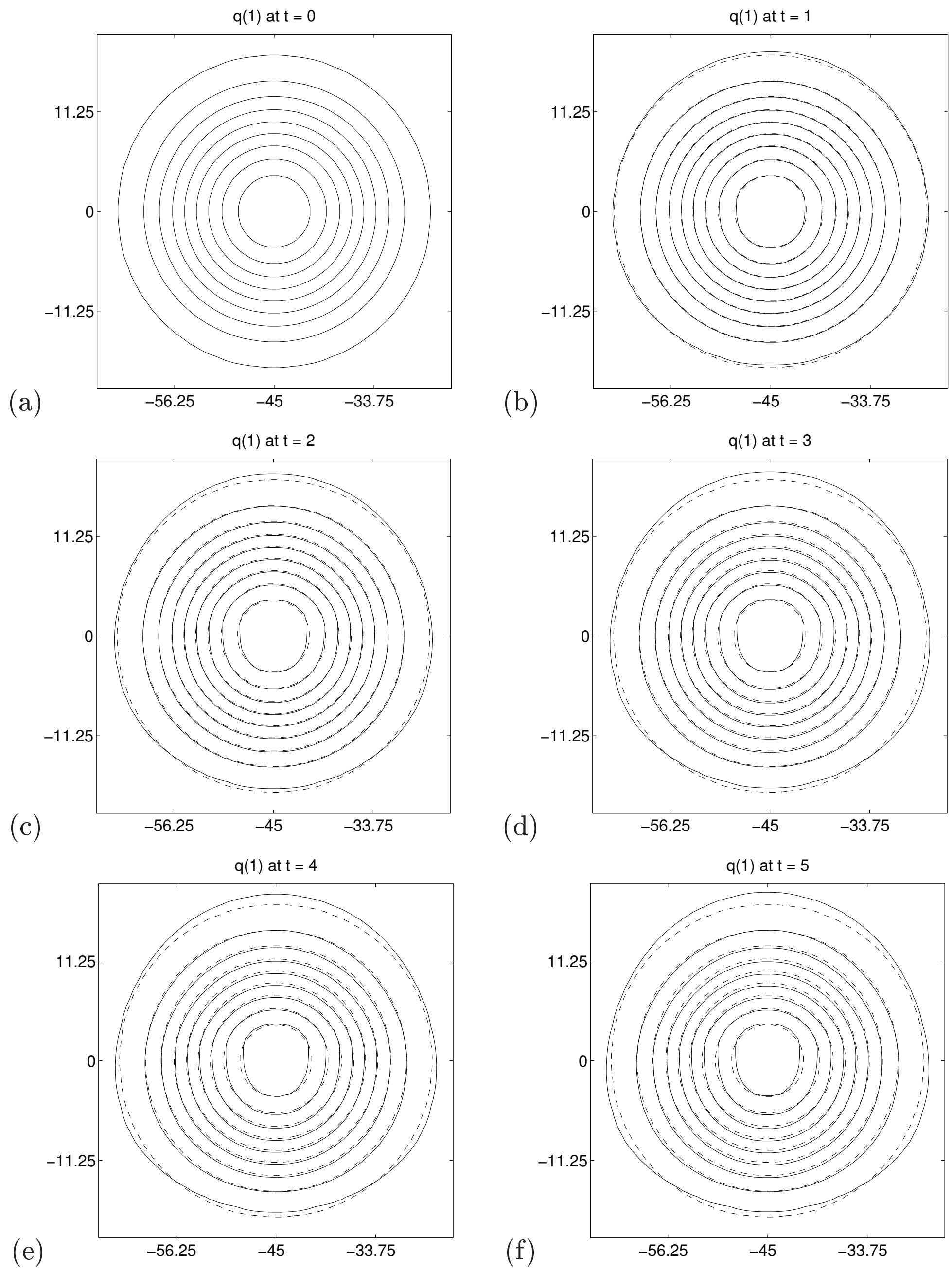

Figure 7.7: The advection of a cosine bell over the poles. Shown are (a) the initial concentration, the solution after (b) one, (c) two (d) three, (e) four and (f) five full revolutions. Plotted are 10 contour lines from $q = 0.015$ to $q = 1$ where the dashed lines are the exact solution and the solid lines are the numerical solution.

where

$$s(\phi,\lambda) \equiv \mathbf{dist}\big[\,(\phi,\lambda) \leftrightarrow (-\pi/4,0)\,\big] = r\cos^{-1}\Big\{\cos(\lambda)\cos(\phi+\pi/4)\Big\}\,. \tag{7.43}$$

The streamfunction is chosen so that it produces a velocity field corresponding to solid body rotation over the North and South Poles:

$$\Psi(\phi,\lambda) = -2\pi\cos(\phi-\pi/4)\cos(\lambda)\,. \tag{7.44}$$

The streamlines are shown in Figure 7.6.

The streamfunction is scaled so that after one unit of time the initial cosine bell has made one full revolution around the sphere. The grid resolution is $90\times 90\times 6$, meaning that each of the six grid patches has a resolution of 90×90. The solutions to this problem at $t = 0, 1, 2, 3, 4$, and 5 are shown in Figure 7.7. Even after five full rotations we find that the numerical solution is in good agreement with the exact solution.

7.3.2 Example: advection of a discontinuous pattern over the poles

We now attempt the same problem as above but with a tracer concentration that is discontinuous and larger than a single grid patch:

$$q(\phi,\lambda,0) = \begin{cases} 1 & \text{if} \quad \mathbf{dist}\big[\,(\phi,\lambda)\leftrightarrow(-\pi/4,0)\,\big] < 0.4 \\ 1 & \text{if} \quad 0.72 < \mathbf{dist}\big[\,(\phi,\lambda)\leftrightarrow(-\pi/4,0)\,\big] < 1.12 \\ 0 & \text{otherwise}\,. \end{cases} \tag{7.45}$$

In Figure 7.8 the solution is shown at time $t = 0, 1$, and 5. Although some numerical dissipation is apparent near the discontinuities of the advected pattern, the approximate solution remains accurate even after five full rotations.

In order to verify our earlier claim that mass is conserved by our numerical method and our treatment of the artificial boundaries, we have computed in Figure 7.9 the deviation of the total mass from the initial mass as a function of time. In both examples the loss of mass is at the level of the numerical round-off error.

7.4 Shallow water on the sphere

The shallow water equations from hydrodynamics can be simply obtained by setting $B_1 = B_2 = 0$ in the SMHD equations. The shallow water equations in generalized coordinates are given by

$$\partial_t \begin{bmatrix} h \\ hu_1 \\ hu_2 \end{bmatrix} + \frac{1}{\kappa}\partial_\xi\left(\kappa\begin{bmatrix} hu_1 \\ \mathfrak{T}_{11} \\ \mathfrak{T}_{12}\end{bmatrix}\right) + \frac{1}{\kappa}\partial_\eta\left(\kappa\begin{bmatrix} hu_2 \\ \mathfrak{T}_{21} \\ \mathfrak{T}_{22}\end{bmatrix}\right) = \begin{bmatrix} 0 \\ -\Gamma^1_{mn}\mathfrak{T}_{mn} \\ -\Gamma^2_{mn}\mathfrak{T}_{mn}\end{bmatrix}, \tag{7.46}$$

where summation is implied on m and n in the source term and the components of the momentum tensor ($\mathfrak{T}$) are given by

$$\mathfrak{T}_{mn} \equiv hu_m u_n + \frac{1}{2}gh^2\boldsymbol{h}^{-1}_{mn}\,. \tag{7.47}$$

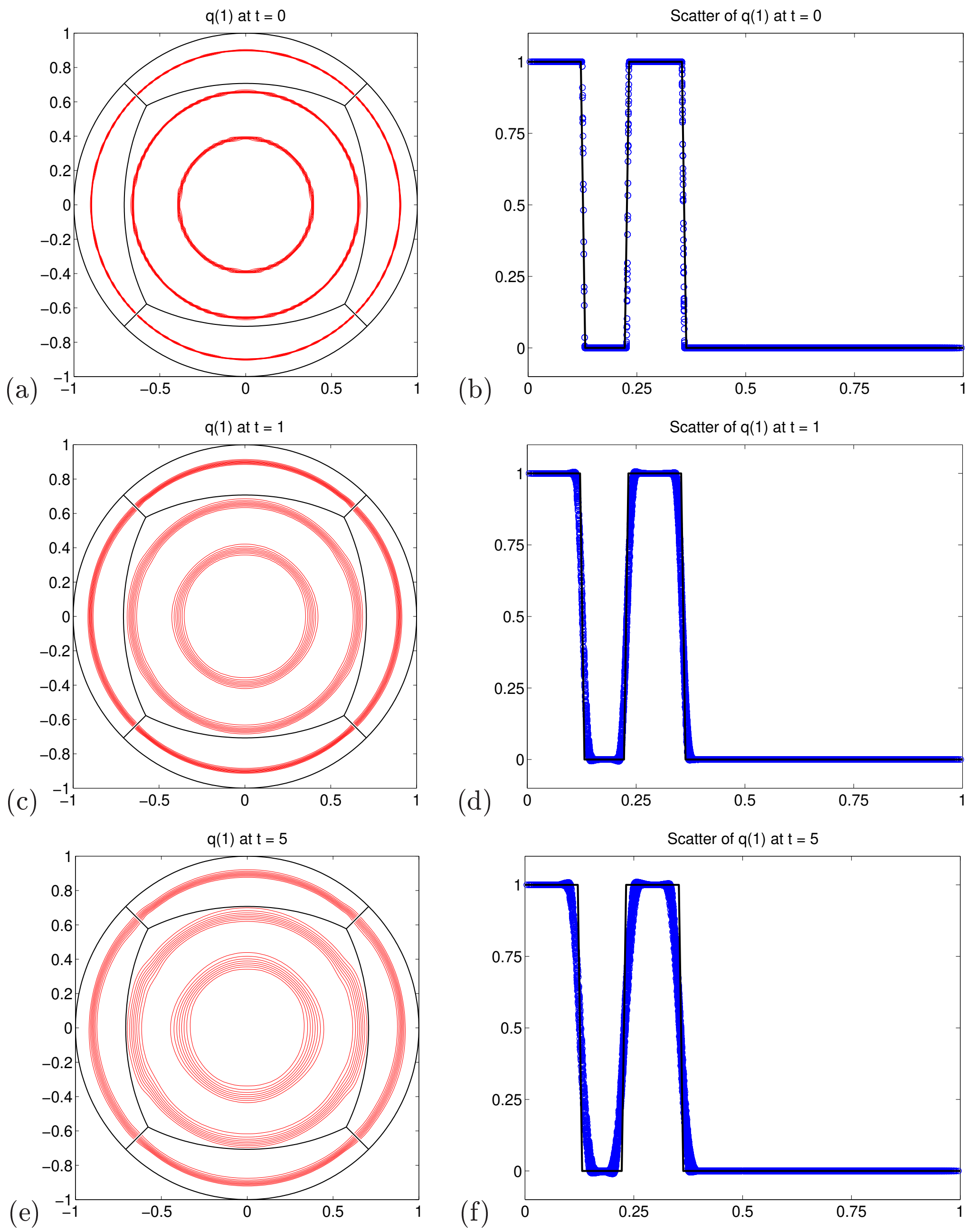

Figure 7.8: The advection of a discontinuous profile over the poles. Shown are (a) a contour plot and (b) a scatter plot of the initial concentrations, (c) a contour plot and (d) a scatter plot of the solution after one full revolution, and (e) a contour plot and (f) a scatter plot of the solution after five full revolutions.

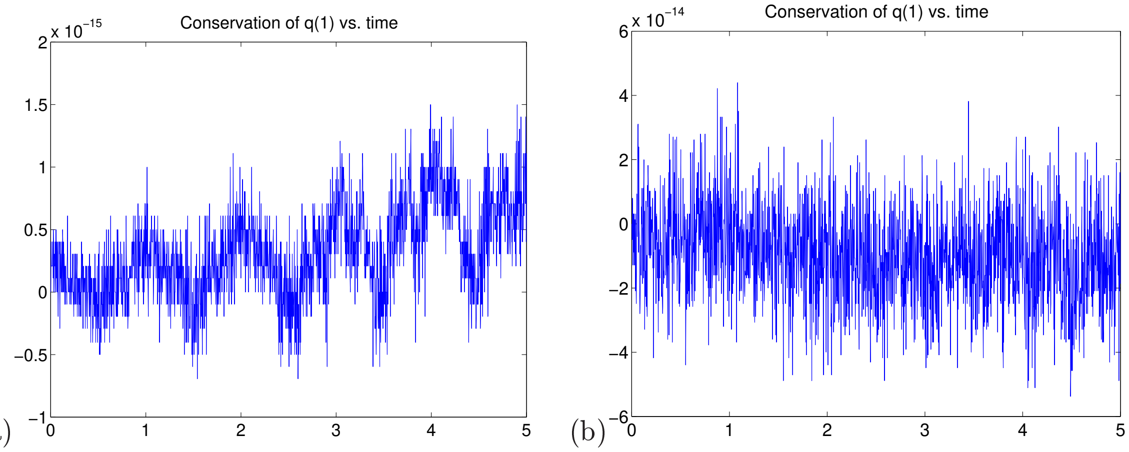

Figure 7.9: A plot of the total concentration minus the initial concentration as a function of time for (a) the advection of a cosine bell example and (b) the advection of discontinuous profile example.

This set of equations has been historically used as a simplified model of atmosphere and ocean dynamics (see [19, 28, 68]).

7.4.1 The Coriolis force

The rotation of the Earth is an important element in the dynamics of the atmosphere and ocean. Without loss of generality we let the axis of rotation be the Cartesian z-axis. If we solve the shallow water equations in the reference frame of the rotating Earth, we introduce in the momentum equations a *pseudo-force* of the form

$$\boldsymbol{\psi}_f \equiv -2\Omega\,\hat{\mathbf{k}} \times \mathbf{u} - \Omega\,\hat{\mathbf{k}} \times \left(\Omega\,\hat{\mathbf{k}} \times \boldsymbol{r}\right)\,, \tag{7.48}$$

where Ω is the rotation rate, $\hat{\mathbf{k}}$ is the unit vector in the z-direction, and $\boldsymbol{r}$ is the position vector (i.e., $\boldsymbol{r} = (x, y, z)$ in Cartesian coordinates). The first term in the above expression is referred as the *Coriolis force* and the second term is the *centrifugal force*. In order to keep matter from flying off of the surface of the Earth, the centrifugal force and the gravitational force must be in balance. Therefore, for flows that are confined to the surface of the Earth only the Coriolis force will affect the dynamics and we can write:

$$\boldsymbol{\psi}_f \equiv -f\hat{\mathbf{k}} \times \mathbf{u}\,, \tag{7.49}$$

where $f = 2\Omega$ is the Coriolis parameter [19]. The Coriolis force written in Cartesian, spherical, and cubed sphere coordinates is given below:

$$\textbf{Cartesian:} \quad \boldsymbol{\psi}_f = \begin{bmatrix} fhu_y \\ -fhu_x \end{bmatrix} \tag{7.50}$$

$$\textbf{Spherical:} \quad \boldsymbol{\psi}_f = f\tan(\lambda)\begin{bmatrix} hu_\lambda \\ -\cos^2(\lambda)\, hu_\phi \end{bmatrix} \tag{7.51}$$

$$\textbf{Cubed Sphere:} \quad \boldsymbol{\psi}_f = \frac{f\sin(\lambda(\xi,\eta))}{\kappa}\begin{bmatrix} \boldsymbol{h}_{21}hu_1 + \boldsymbol{h}_{22}hu_2 \\ -\boldsymbol{h}_{11}hu_1 - \boldsymbol{h}_{21}hu_2 \end{bmatrix}. \tag{7.52}$$

7.4.2 The longitudinally symmetric equations

In order to test the accuracy of the wave propagation method in generalized coordinates we would like to compare to a one-dimensional symmetric solution. In particular, let us consider the shallow water equations in spherical coordinates under the assumption that the solution is independent of longitude:

$$\partial_\phi h = \partial_\phi u_\phi = \partial_\phi u_\lambda = 0. \tag{7.53}$$

Under this assumption the shallow water equations reduce to the following set of equations:

$$\partial_t \begin{bmatrix} h \\ hu_\phi \\ hu_\lambda \end{bmatrix} + \partial_\lambda \begin{bmatrix} hu_\lambda \\ hu_\phi u_\lambda \\ hu_\lambda^2 + \frac{1}{2}gh^2 \end{bmatrix} = \psi(q,\lambda)\,, \tag{7.54}$$

where

$$\psi(q,\lambda) = \tan(\lambda)\begin{bmatrix} hu_\lambda \\ 3hu_\phi u_\lambda \\ hu_\lambda^2 - \cos^2(\lambda)hu_\phi^2 \end{bmatrix} + \begin{bmatrix} 0 \\ fhu_\lambda\tan(\lambda) \\ -fhu_\phi\cos\lambda\sin\lambda \end{bmatrix}. \tag{7.55}$$

7.4.3 Example: adjustment on a non-rotating sphere

The first example we consider is an adjustment or "dam break" problem on a non-rotating ($f = 0$) sphere. We begin with an initially quiescent flow with a height anomaly centered at the North Pole:

$$q(\phi,\lambda,0) = \begin{cases} 1 & \text{if} \quad \textbf{dist}\big[\,(\phi,\lambda) \leftrightarrow (0,\pi/2)\,\big] < \pi/5 \\ 0.1 & \text{if} \quad \textbf{dist}\big[\,(\phi,\lambda) \leftrightarrow (0,\pi/2)\,\big] > \pi/5 \end{cases} \tag{7.56}$$

$$u_1(\phi,\lambda,0) = 0 \tag{7.57}$$

$$u_2(\phi,\lambda,0) = 0\,. \tag{7.58}$$

The solution to the shallow water equations on a $90 \times 90 \times 6$ grid at various times is shown in scatter plot format in Figure 7.10(a)-(c). The cubed sphere solution accurately maintains the shock structure and symmetry, even across grid interfaces. In Figure 7.10(d) we verify that the mass is numerically conserved.

7.4.4 Example: adjustment on a rotating sphere

We now repeat the above experiment but with a Coriolis force source term with $f = 4$:

$$\psi(q,\xi,\eta) = \frac{f\sin(\lambda(\xi,\eta))}{\kappa}\begin{bmatrix} 0 \\ \boldsymbol{h}_{21}hu_1 + \boldsymbol{h}_{22}hu_2 \\ -\boldsymbol{h}_{11}hu_1 - \boldsymbol{h}_{21}hu_2 \end{bmatrix}. \tag{7.59}$$

We use the Strang splitting approach to handle the source term (see Chapter 2). The solution to this problem on a $90 \times 90 \times 6$ grid at various times is shown in scatter plot format in Figure 7.11(a)-(c). The cubed sphere solution accurately maintains the shock structure and symmetry, even across grid interfaces. In Figure 7.11(d) we verify that the mass is numerically conserved.

7.4.5 Example: flow past an isolated mountain

As a final example of the shallow water equations on the surface of a sphere we consider a problem similar to test #5 of the Williamson et al. [93] test suite. We place an isolated mountain that is conical in shape at 90°E longitude and 30°N latitude. In particular, the bottom topography is given by

$$b(\phi,\lambda) = \frac{1}{2}\left(1 - a(\phi,\lambda)/A\right), \tag{7.60}$$

where $A = 20^\circ = \pi/9$ and

$$a(\phi,\lambda) = \sqrt{\min\left(A^2, (\phi-\pi/2)^2 + (\lambda-\pi/6)^2\right)}. \tag{7.61}$$

If we define the total height of the fluid interface to be

$$H(\phi,\lambda,t) \equiv h(\phi,\lambda,t) + b(\phi,\lambda), \tag{7.62}$$

then the initial conditions are

$$H(\phi,\lambda,0) = 1 \tag{7.63}$$

$$u_\phi(\phi,\lambda,0) = 1 \tag{7.64}$$

$$u_\lambda(\phi,\lambda,0) = 0. \tag{7.65}$$

The resulting topographic source term,

$$\psi_b(q,\xi,\eta) = \begin{bmatrix} 0 \\ -gh\,\partial_\xi b \\ -gh\,\partial_\eta b \end{bmatrix}, \tag{7.66}$$

is handled through the Strang splitting approach. The partial derivatives of $b(\xi,\eta)$ are computed using the following centered finite difference approximation:

$$\left[\partial_\xi b\right]_{ij} \approx \frac{b(\xi_i + 0.005\Delta\xi, \eta_j) - b(\xi_i - 0.005\Delta\xi, \eta_j)}{0.01\Delta\xi} \tag{7.67}$$

$$\left[\partial_\eta b\right]_{ij} \approx \frac{b(\xi_i, \eta_j + 0.005\Delta\eta) - b(\xi_i, \eta_j - 0.005\Delta\eta)}{0.01\Delta\eta}. \tag{7.68}$$

We solve this problem on a $90 \times 90 \times 6$ grid. The results of this computation are shown in Figures 7.12 and 7.13. These plots demonstrate the effect of a large mountain on a flow that in the absence of topography would be in steady-state.

7.5 Shallow water magnetohydrodynamics on the sphere

The final system of partial differential equations we consider on the surface of a sphere are the shallow water magnetohydrodynamic (SMHD) equations:

$$\partial_t \begin{bmatrix} h \\ hu_1 \\ hu_2 \\ hB_1 \\ hB_2 \end{bmatrix} + \frac{1}{\kappa}\partial_\xi \left(\kappa \begin{bmatrix} hu_1 \\ \mathfrak{T}_{11} \\ \mathfrak{T}_{12} \\ \mathfrak{X}_{11} \\ \mathfrak{X}_{12} \end{bmatrix} \right) + \frac{1}{\kappa}\partial_\eta \left(\kappa \begin{bmatrix} hu_2 \\ \mathfrak{T}_{21} \\ \mathfrak{T}_{22} \\ \mathfrak{X}_{21} \\ \mathfrak{X}_{22} \end{bmatrix} \right) = \begin{bmatrix} 0 \\ -\Gamma^1_{mn}\mathfrak{T}_{mn} \\ -\Gamma^2_{mn}\mathfrak{T}_{mn} \\ 0 \\ 0 \end{bmatrix} \tag{7.69}$$

$$\partial_\xi \left(\kappa h B_1\right) + \partial_\eta \left(\kappa h B_2\right) = 0\,, \tag{7.70}$$

where

$$\mathfrak{T}_{mn} \equiv hu_m u_n - hB_m B_n + \frac{1}{2} g h^2 \boldsymbol{h}^{-1}_{mn} \tag{7.71}$$

$$\mathfrak{X}_{mn} \equiv hu_m B_n - hu_n B_m\,. \tag{7.72}$$

As was discussed in Chapter 6, if we are to use the MPACT scheme in generalized coordinates we will also need to solve the following advection equation for the magnetic potential:

$$\partial_t \left(\kappa \mathbb{A}\right) + \kappa_s u_1 \partial_\xi \mathbb{A} + \kappa_s u_2 \partial_\eta \mathbb{A} = 0\,. \tag{7.73}$$

Note that if we are solving on a sphere of radius r, then $\kappa = r\kappa_s = \sqrt{h_{11}h_{22} - h_{12}^2}$. We will apply interpolating boundary conditions (Option 2) to both the SMHD equations and the magnetic potential advection equation.

7.5.1 The longitudinally symmetric equations

In order to verify the correctness of our cubed sphere solution we again would like to compare to a one-dimensional symmetric equation. The longitudinally symmetric SMHD equations are given by

$$\partial_t \begin{bmatrix} h \\ hu_\phi \\ hu_\lambda \\ hB_\phi \\ hB_\lambda \end{bmatrix} + \partial_\lambda \begin{bmatrix} hu_\lambda \\ hu_\phi u_\lambda - hB_\phi B_\lambda \\ hu_\lambda^2 - hB_\lambda^2 + \frac{1}{2}gh^2 \\ hu_\lambda B_\phi - hu_\phi B_\lambda \\ 0 \end{bmatrix} = \psi(q,\lambda) \tag{7.74}$$

$$\partial_\lambda \left(hB_\lambda\right) = 0\,, \tag{7.75}$$

where

$$\psi(q,\lambda) = \tan(\lambda) \begin{bmatrix} hu_\lambda \\ 3(hu_\phi u_\lambda - hB_\phi B_\lambda) \\ (hu_\lambda^2 - hB_\lambda^2) - \cos^2(\lambda)(hu_\phi^2 - hB_\phi^2) \\ hu_\lambda B_\phi - hu_\phi B_\lambda \\ 0 \end{bmatrix}\,. \tag{7.76}$$

7.5.2 Example: a longitudinally symmetric solution

We consider an example with the following initial conditions:

$$h(\phi,\lambda,0) = 0.5 \tag{7.77}$$

$$u_1(\phi,\lambda,0) = 0 \tag{7.78}$$

$$u_2(\phi,\lambda,0) = 0 \tag{7.79}$$

$$\mathbb{A}(\phi,\lambda,0) = \begin{cases} 0.942809950511461972 & \text{if} \quad 5\pi/48 \leq \lambda \leq \pi/2 \\ 2364 + I(\lambda) & \text{if} \quad -11\pi/48 \leq \lambda \leq 5\pi/48 \\ 0.564868582895320923 & \text{if} \quad -\pi/2 \leq \lambda \leq -11\pi/48\,, \end{cases} \tag{7.80}$$

where

$$I(\lambda) = \int \cos(\lambda)\left(\frac{3}{4} - \frac{66}{\pi^2}\left(\lambda + \frac{\pi}{16}\right)^2 + \frac{1836}{\pi^4}\left(\lambda + \frac{\pi}{16}\right)^4 - \frac{15552}{\pi^6}\left(\lambda + \frac{\pi}{16}\right)^6\right) d\lambda\,. \tag{7.81}$$

The above initial conditions were chosen so that $\mathbb{A}$ has at least two continuous derivatives and $\mathfrak{B}$ has at least one continuous derivative for all $\lambda \in [-\pi/2, \pi/2]$.

The solution to this problem on a $90 \times 90 \times 6$ grid is shown in Figures 7.14, 7.15, and 7.16. A scatter plot at various times of the height is shown in Figure 7.14, the longitudinal (hB_ϕ) component of the magnetic field in Figure 7.15, and the latitudinal (hB_λ) component of the magnetic field in Figure 7.16. The hB_ϕ and hB_λ values at cell centers are obtained by applying the cubed sphere Jacobian matrices to the following vector:

$$\mathfrak{B}_{ij} = \frac{1}{2}\begin{bmatrix} [\mathfrak{b}_1]_{i+1/2,j} + [\mathfrak{b}_1]_{i-1/2,j} \\ [\mathfrak{b}_2]_{i,j+1/2} + [\mathfrak{b}_2]_{i,j-1/2} \end{bmatrix}. \tag{7.82}$$

The cubed sphere solution matches the one-dimensional solution quite well. There is some noise introduced into the hB_λ component of the magnetic field which in the exact solution should be identically zero for all time. This error is due to the fact that we are imposing a discrete divergence on $\mathfrak{b}_1$ and $\mathfrak{b}_2$ at cell edges and not on hB_ϕ and hB_λ at cell centers. Overall, however, the cubed sphere solution accurately maintains the shock structure and the symmetry of the flow.

In Figure 7.17 we demonstrate that the mass is numerically conserved and that the divergence of the magnetic field is of the same magnitude as the round-off error.

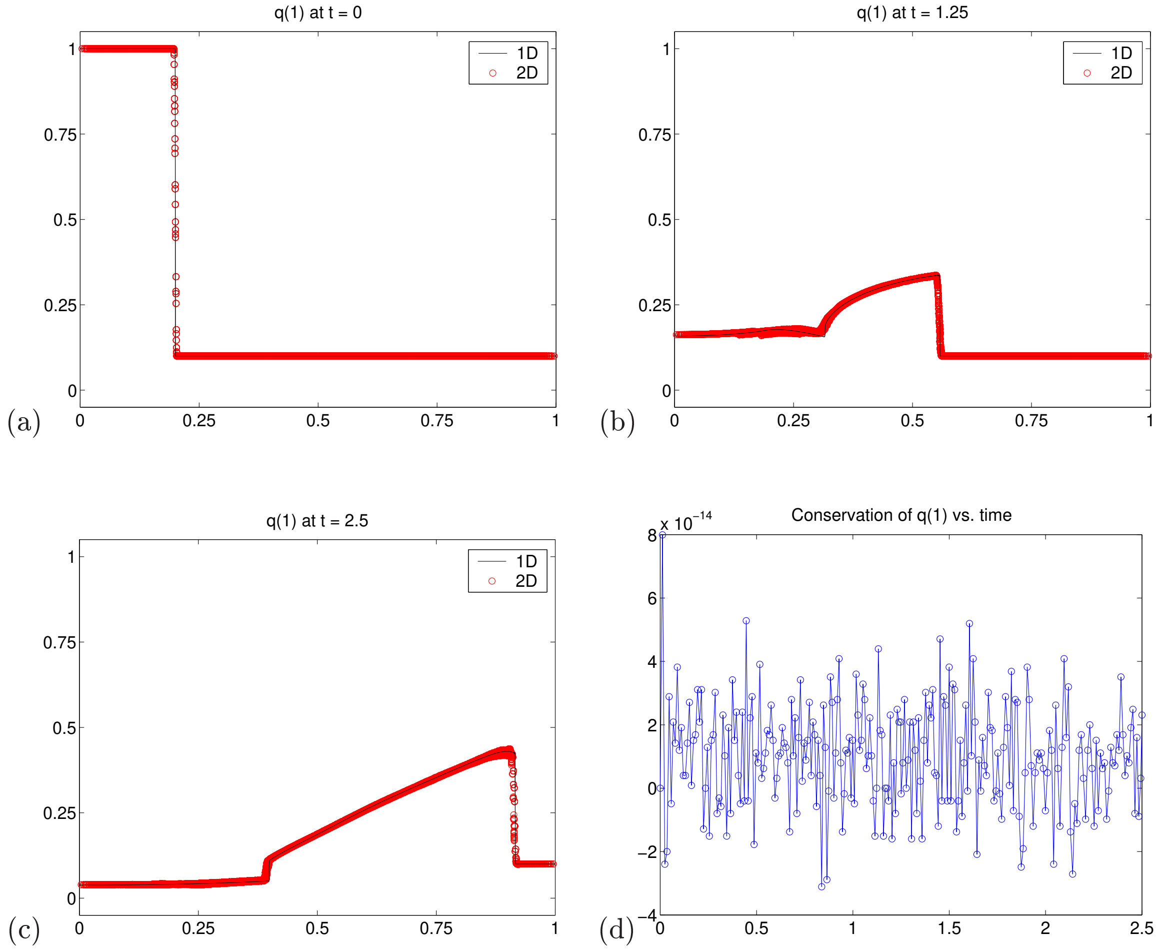

Figure 7.10: Adjustment of a height anomaly at the North Pole on a non-rotating sphere ($f = 0$). The flow should remain independent of the longitude. Shown are a scatter plot of the height at time (a) $t = 0$, (b) $t = 1.25$, and (c) $t = 2.5$. A plot of the total mass at time t minus the initial mass is shown in plot (d).

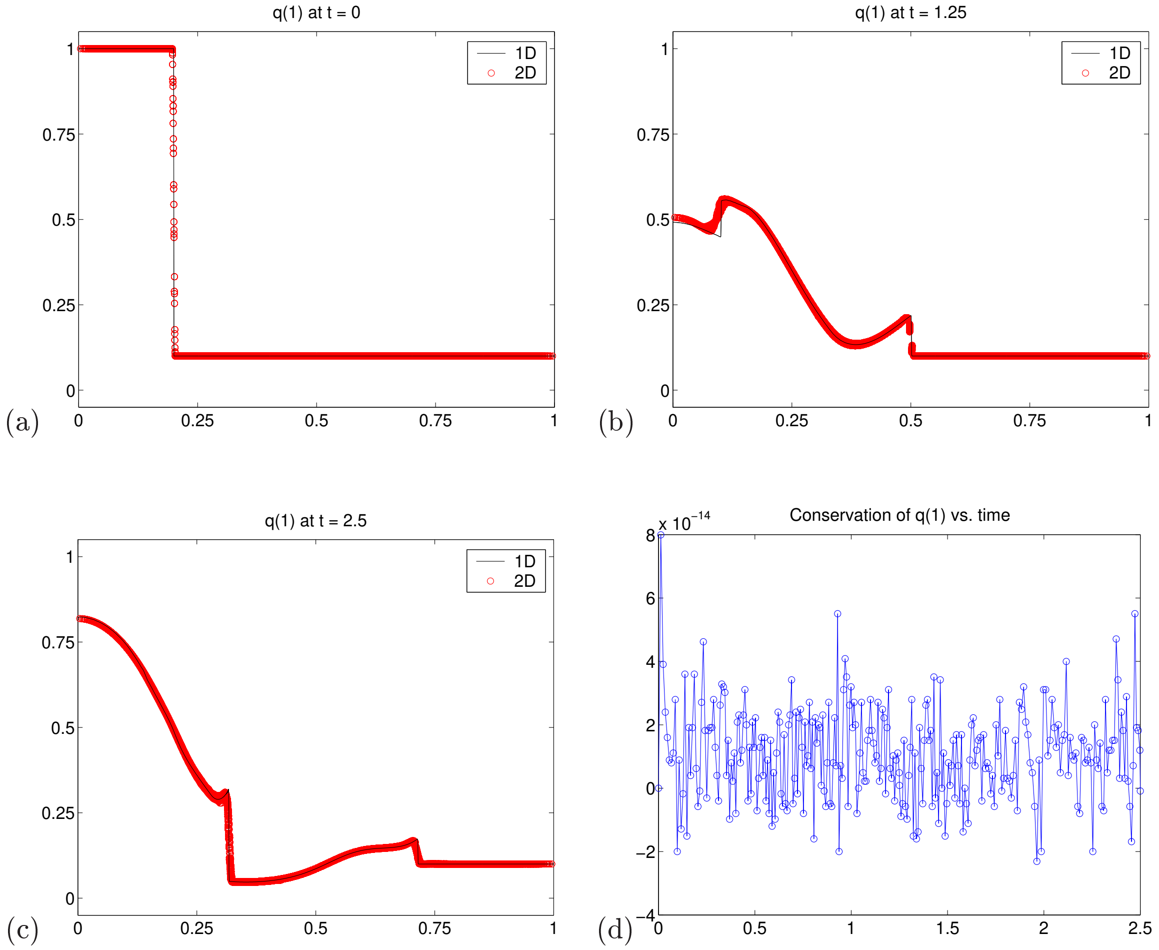

Figure 7.11: Adjustment of a height anomaly at the North Pole on a rotating sphere ($f = 4$). The flow should remain independent of the longitude. Shown are a scatter plot of the height at time (a) $t = 0$, (b) $t = 1.25$, and (c) $t = 2.5$. A plot of the total mass at time t minus the initial mass is shown in plot (d).

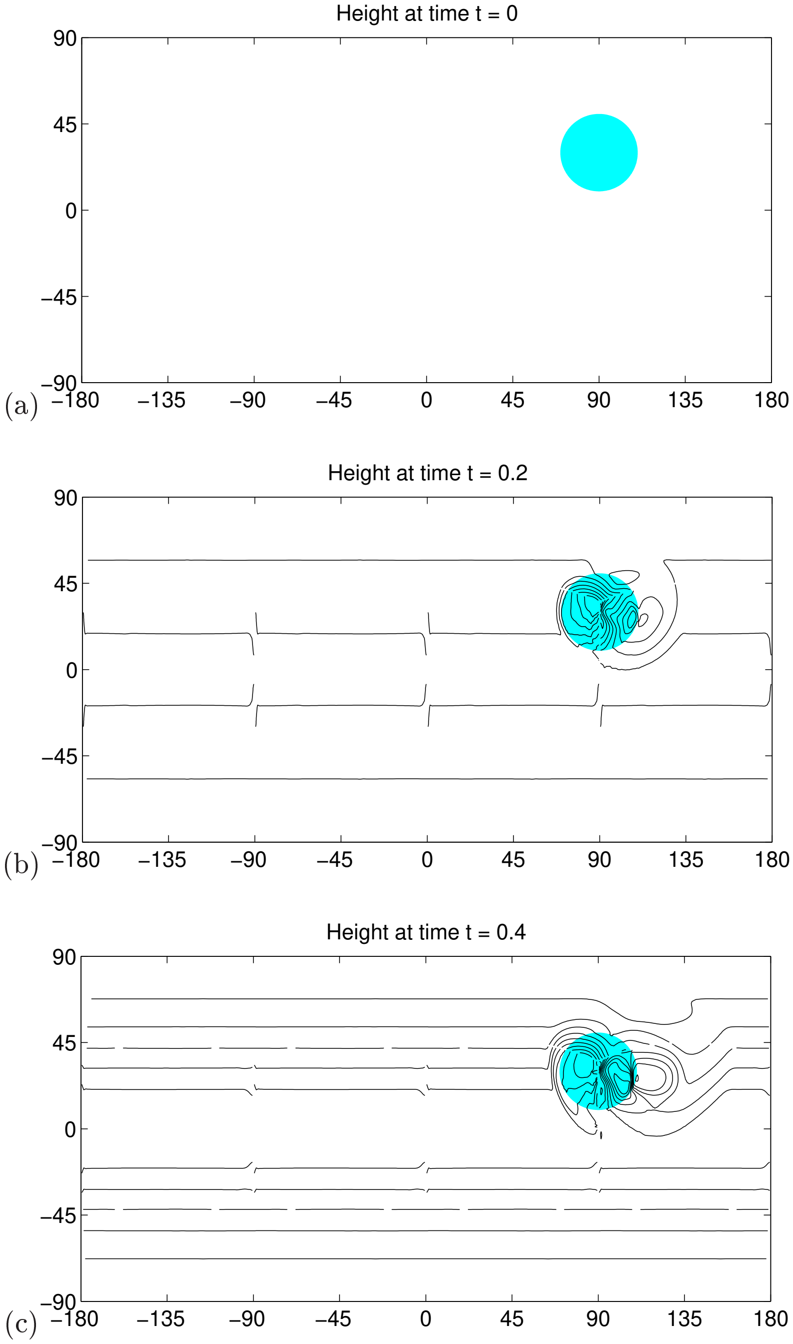

Figure 7.12: Shallow water flow over an isolated mountain centered at 90°E longitude and 30°N latitude. Shown is the total height $(h + b)$ at time (a) $t = 0$, (b) $t = 0.2$, and (c) $t = 0.4$. There are slight irregularities in the contour lines which occur due to the visualization package.

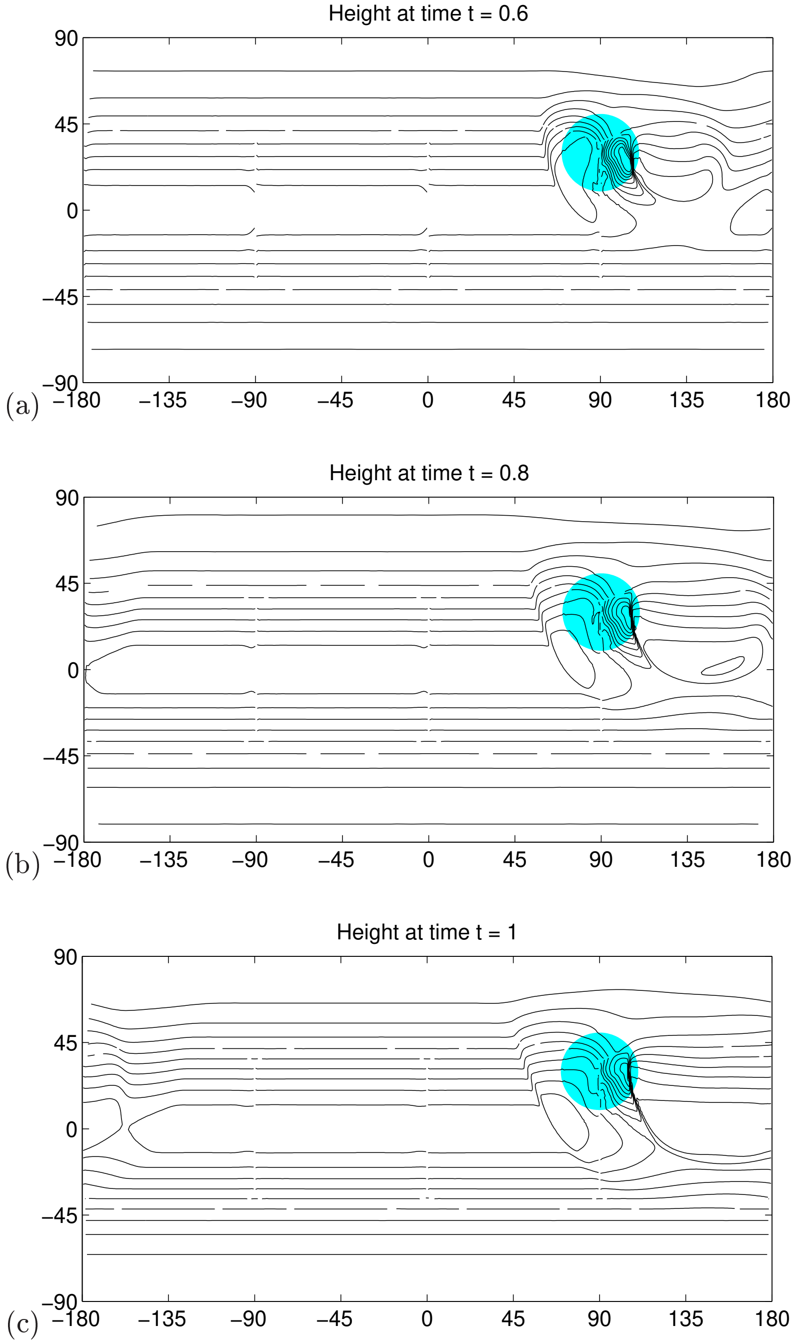

Figure 7.13: Shallow water flow over an isolated mountain centered at 90°E longitude and 30°N latitude. Shown is the height $(h + b)$ at time (a) $t = 0.6$, (b) $t = 0.8$, and (c) $t = 1.0$. There are slight irregularities in the contour lines which occur due to the visualization package.

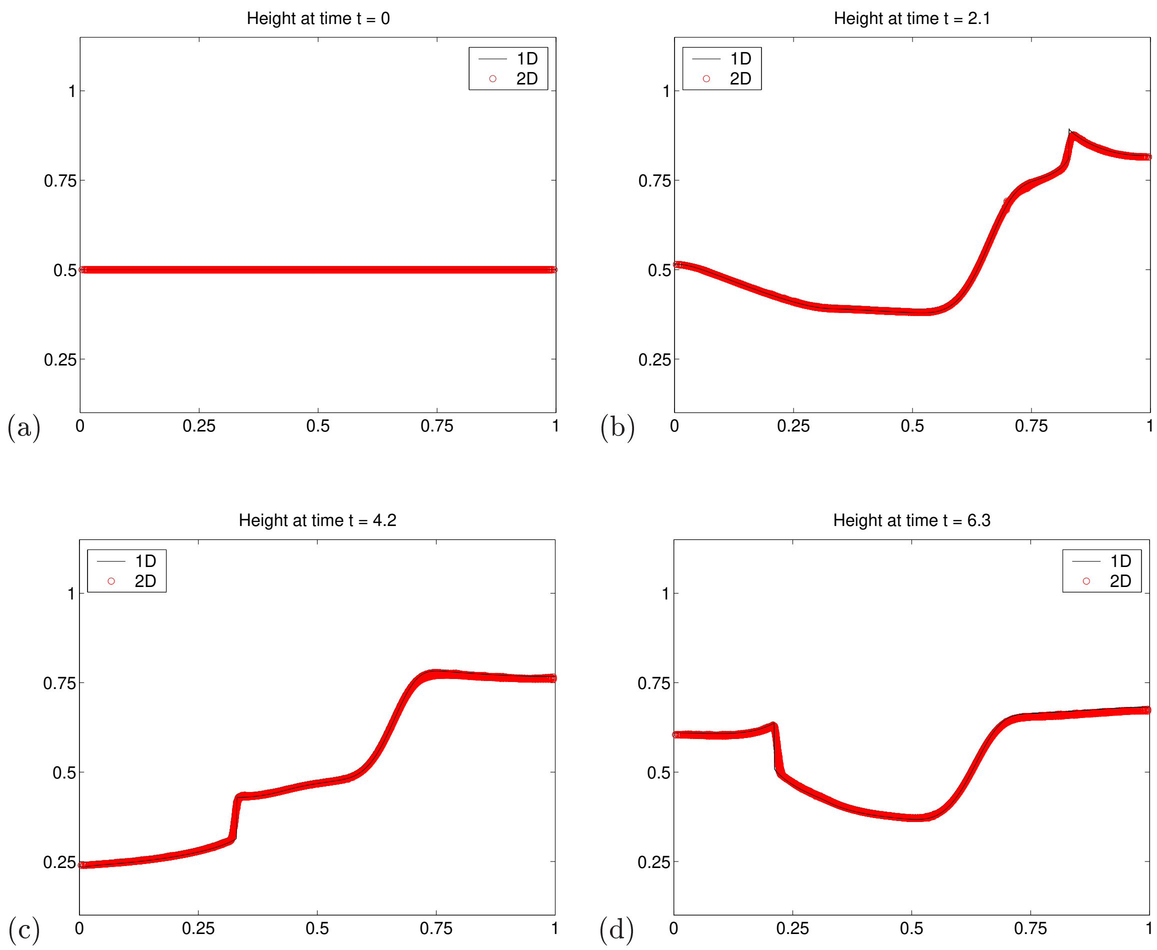

Figure 7.14: A longitudinally symmetric solution to the SMHD equations on the surface of a sphere. Shown are a scatter plot of the height at time (a) $t = 0$, (b) $t = 2.1$, (c) $t = 4.2$, and (d) $t = 6.3$.

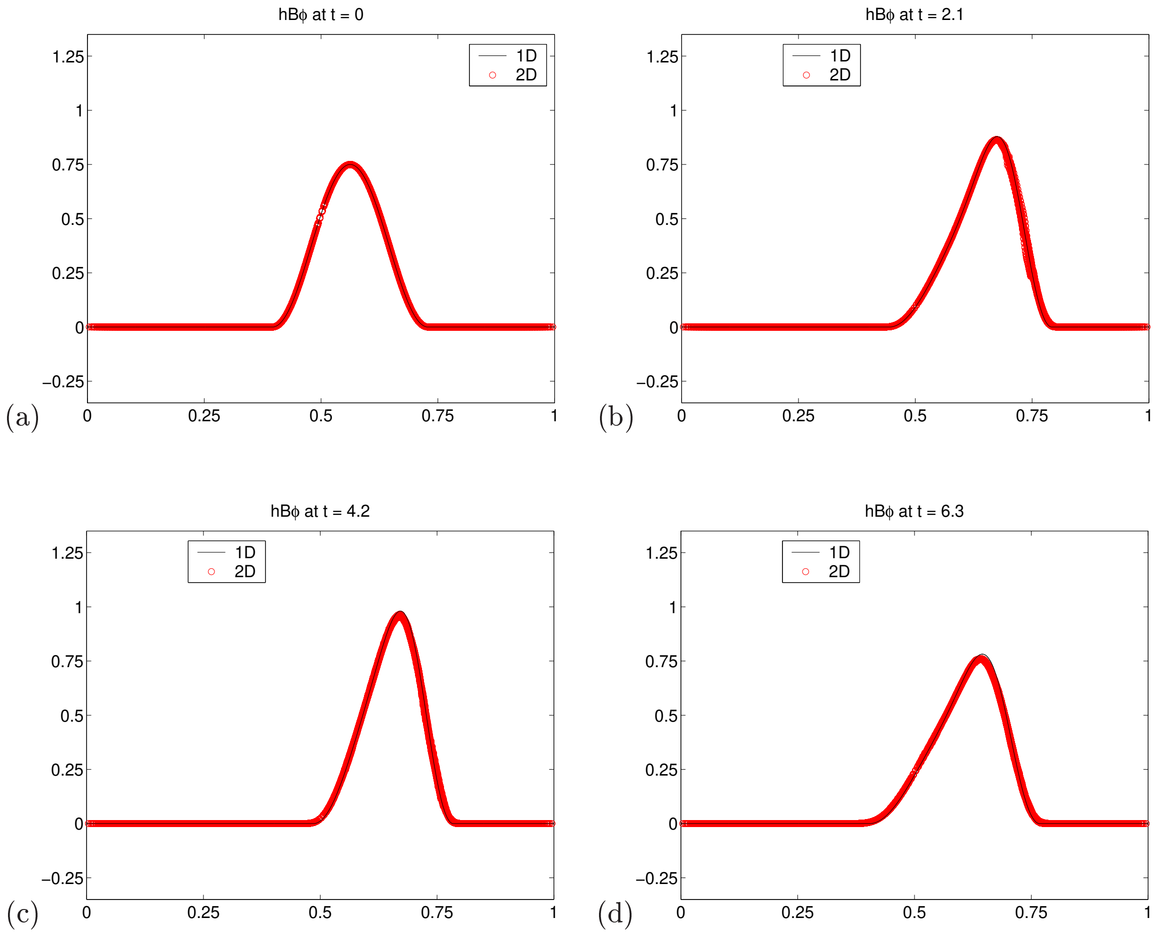

Figure 7.15: A longitudinally symmetric solution to the SMHD equations on the surface of a sphere. Shown are a scatter plot of the longitudinal component of the magnetic field at time (a) $t = 0$, (b) $t = 2.1$, (c) $t = 4.2$, and (d) $t = 6.3$.

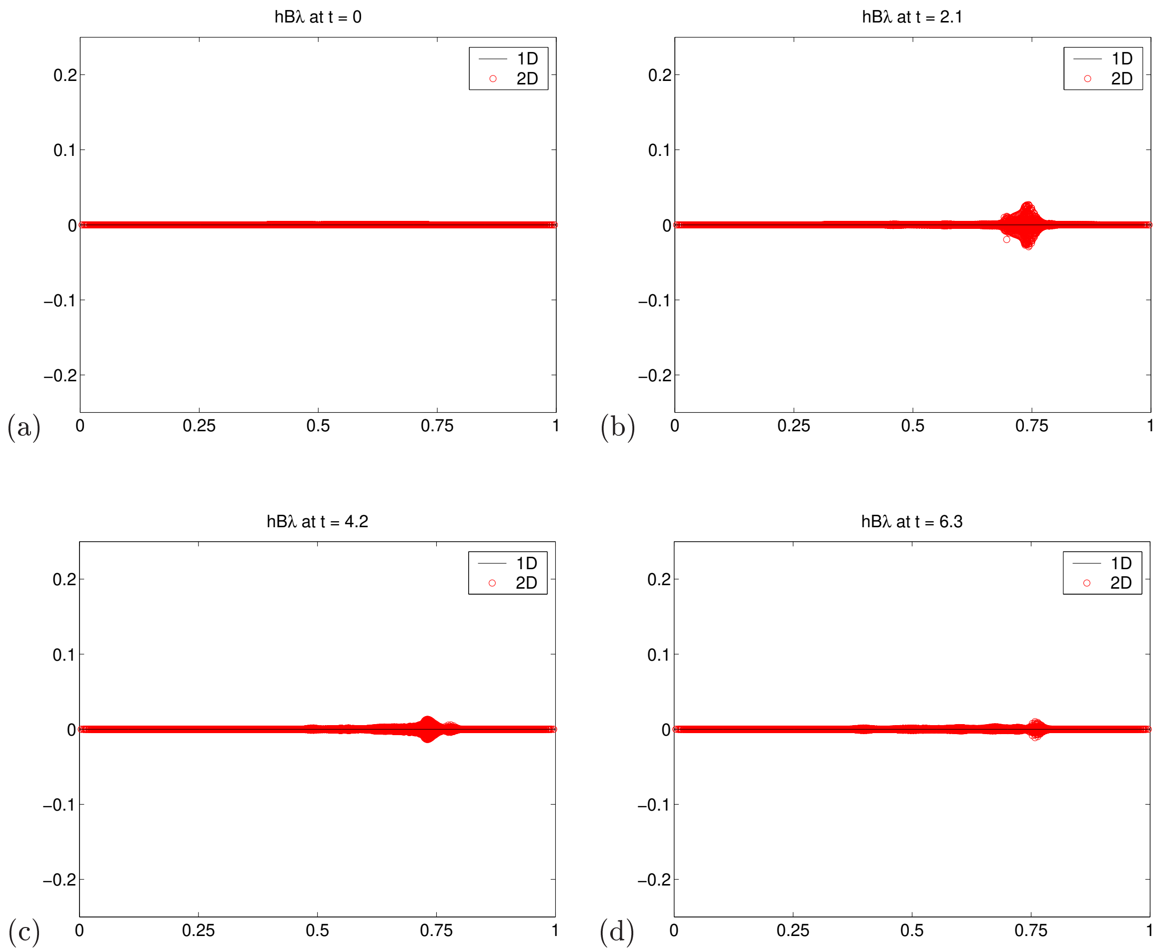

Figure 7.16: A longitudinally symmetric solution to the SMHD equations on the surface of a sphere. Shown are a scatter plot of the latitudinal component of the magnetic field at time (a) $t = 0$, (b) $t = 2.1$, (c) $t = 4.2$, and (d) $t = 6.3$.

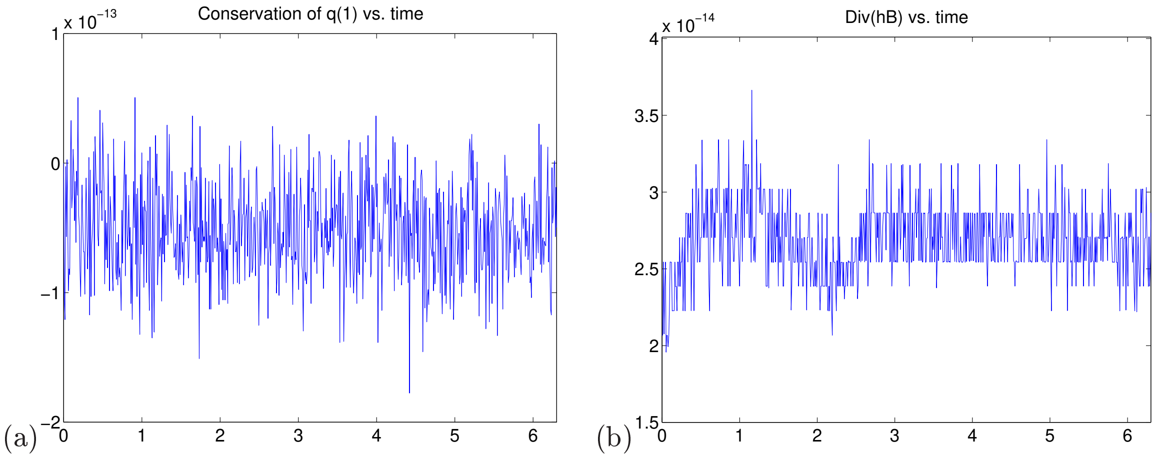

(a) (b)

Figure 7.17: Plots from the longitudinally symmetric SMHD example showing (a) the total mass minus the initial mass as a function of time and (b) the divergence of the magnetic field as function of time.